Environ Earth Sci (2016) 75:206
DOI 10.1007/s12665-015-4920-7

ORIGINAL ARTICLE

A finite volume method for two-phase debris flow simulation that accounts for the pore-fluid pressure evolution

Wei Liu[1] · Siming He[1,2,3] · Xinpo Li[1,2]

Received: 13 March 2015 / Accepted: 10 August 2015 / Published online: 25 January 2016

Abstract The temporal and spatial evolution of pore-fluid pressure exerts strong control on debris flow motion because it can counteract normal stresses at grain contacts, reduce friction, and enhance bulk flow mobility. In Iverson's two-phase debris flow model, the depth-averaged pore pressure equation, which takes into account the effect of shear-induced dilatancy, was combined with a previous model to describe the simultaneous evolution of flow velocity and depth, solid mass, and pore-fluid pressure. In this work, a high-resolution scheme based on the finite volume method was used to solve the system of equations. Several numerical tests were performed to verify the ability of the presented model and the accuracy of the proposed numerical method. Numerical results were compared with experimental data obtained in a laboratory, and the effectiveness of the proposed numerical method for solving practical problems has been proven. Numerical results indicated that increases of the pore-fluid pressure could enhance the motion of debris flow and expand the spread area. Furthermore, results showed that the debris shear-induced dilatancy could affect the evolution of pore-fluid pressure, thus further influencing the motion of debris flow.

✉ Xinpo Li
lixinpo@imde.ac.cn

Siming He
hsm@imde.ac.cn

[1] Institute of Mountain Hazards and Environment (IMHE), Chinese Academy of Sciences, Chengdu, China

[2] Key Laboratory of Mountain Hazards and Surface Processes, Chinese Academy of Sciences, Chengdu, China

[3] Center for Excellence in Tibetan Plateau Earth Sciences, Chinese Academy of Sciences, Beijing, China

Keywords Debris flows · Pore-fluid pressure · Finite volume method · Shear-induced dilatancy

Introduction

Debris flows represent one of the most extremely destructive and dangerous types of natural hazards in the world (Begueria et al. 2009; Wu et al. 2009; Hutter and Luca 2012; Luna et al. 2012; Pudasaini 2012). Consequently, there is a significant demand for models that can predict the dynamics, sliding distances, and hazard zones of such events to prevent loss. In recent years, significant progress has been made with regard to physical models and numerical schemes, and these developments have made it possible for researchers to investigate the dynamic processes and assess the risks associated with debris flows (Savage and Hutter 1989; Hungr 1995; Gray et al. 1999; Pudasaini and Hutter 2003; Goren and Aharonov 2009).

Generally, debris flows are multiphase events that consist of a broad distribution of grain sizes mixed with fluid (Pitman et al. 2003; Goren and Aharonov 2007; Wu 2010; George and Iverson 2011; Pudasaini 2012). The behavior of debris flows can vary greatly and will depend on the amount of particle movement, solid–liquid interactions, and the percentage of solid and fluid phases. Iverson and Denlinger (2001) proposed a two-phase model for debris flows by developing a depth-averaged solid–fluid mixture theory based on the assumptions of constant porosity and equality of velocity between fluids and solids. This model suggests that the pore-fluid pressure plays a crucial role in the motion of debris flows because it can counteract normal stresses and thereby reduce friction and enhance bulk flow mobility. Based on research of pore pressure feedback, George and Iverson (2011) proposed a depth-integrated

mathematical model that simulates the coupled evolution of granular dilatancy, pore-fluid pressure, and solid and fluid volume fractions. Results from this model demonstrated that debris dilation causes dissipation of pore pressure, thus further stabilizing debris flow motion. In another work by Pitman and Le (2005), which considered the effect of the drag force on debris flow motion that is caused by the difference of solid and fluid phase velocities, a novel depth-averaged two-fluid model based on the two-fluid equations of Anderson and Jackson (1967) was proposed to describe the interactions between the solid particles and the fluid. More recently, through consideration of the many essential physical phenomena observable in debris flows, Pudasaini (2012) presented a new generalized two-phase debris flow model that takes into account the effects of buoyancy, drag force, and virtual mass.

Several numerical methods have been used for computing the model data for landslides and debris flows over the past few decades, and the main ones include the distinct element method (Preh et al. 2011; Wu and Chen 2011; Zhang et al. 2014; Zhao et al. 2014) and the continuum medium method (Brufau et al. 2004; Pudasaini 2012; Ouyang et al. 2014; Paik 2015). Hsu et al. (2013) used a particle flow code (PFC) based on the discrete element method to study the mechanisms of particle movement in debris flows and determined the contact forces, displacements, and the strength parameters between particles. Wu et al. (2013) studied the post-failure process of the Hsien-du-shan rock avalanche, which was trigged by heavy rainfall, by using discontinuous deformation analysis (DDA). The dynamic behavior that exhibited itself as failure behavior and continuous-progressing failure was well described. However, discrete numerical analysis methods are typically used for simulating the dynamic processes of single-phase, dry granular avalanches, and in such cases, the effect of pore-fluid pressure on the motion of debris flows and the evolution of pore-fluid pressure cannot be exhibited well. In these circumstances, the continuum medium method can be used for simulating the motion of debris flow, and this method has attracted the attention of many researches. George and Iverson (2011) used the finite volume method (FVM) to solve the model equations and the predicted basal pore-fluid pressures matched the measured data relatively well. Furthermore, Pudasaini (2012) used the total variation diminishing non-oscillatory central (TVD-NOC) scheme to solve the model equations and the results were able to highlight the basic physics associated with the contributions of the viscous stresses, virtual mass, generalized drag, and buoyancy and demonstrate the interactions of the solid and fluid phases.

In this study, we investigated Iverson's depth-averaged two-phase debris flow model that accounts for the coupled evolution of the flow dynamics and pore-fluid pressure. This model employs Mohr–Coulomb plasticity for the solid stress, and the fluid stress is modeled as Newtonian viscous stress that formally appears as a single-phase model with a stress term that accounts for the contributions from the two constituents. Pore-fluid pressure has both hydrostatic component and non-hydrostatic component that are established by initial conditions and are dissipated diffusively in response to debris flow motion. A high-resolution scheme based on the finite volume method is presented to solve the system of equations. Finally, with several site-specific examples, we compare the numerical results with experimental data to verify the numerical method and model. In this study, the effect of pore-fluid pressure on the movement of debris flows is discussed. A discussion of the influence of shear-induced dilatancy on the evolution of pore-fluid pressure is also presented.

Model equations

The two-dimensional (2-D), depth-integrated, and mass-conservation equation for a debris flow mixture may be expressed as follows:

$$\rho\left[\frac{\partial h}{\partial t}+\frac{\partial(hu)}{\partial x}+\frac{\partial(hv)}{\partial y}\right]=0 \tag{1}$$

where $\rho=\vartheta_f\rho_f+\left(1-\vartheta_f\right)\rho_s$ is the density; ρ_f is the fluid phase density; ρ_s is the solid phase density; ϑ_f is the fluid volume fraction; h is the height; u and v are the velocity components in the x and y directions, respectively; x represents the horizontal direction; y represents the vertical direction; and t is the time. The depth-integrated x-direction momentum-conservation equation for the grain–fluid mixture of the debris flow may be expressed as (Iverson and Denlinger 2001)

$$\begin{aligned}&\rho\left[\frac{\partial(hu)}{\partial t}+\frac{\partial(hu^2)}{\partial x}+\frac{\partial(huv)}{\partial y}\right]\\&=\rho g_x h-\mathrm{sgn}(u)(\rho g_z h-p_{\mathrm{bed}})\left(1+\frac{u^2}{r_x g_z}\right)\tan\phi_{\mathrm{bed}}\\&\quad+\vartheta_f\mu h\frac{\partial^2 u}{\partial y^2}-\mathrm{sgn}\left(\frac{\partial u}{\partial y}\right)hk_{\mathrm{ap}}\frac{\partial(\rho g_z h-p_{\mathrm{bed}})}{\partial y}\sin\phi_{\mathrm{int}}\\&\quad-3\vartheta_f\mu\frac{u}{h}+\vartheta_f\mu h\frac{\partial^2 u}{\partial x^2}-hk_{\mathrm{ap}}\frac{\partial(\rho g_z h-p_{\mathrm{bed}})}{\partial x}-h\frac{\partial p_{\mathrm{bed}}}{\partial x}\end{aligned} \tag{2}$$

where μ is the pore-fluid viscosity; $r=(r_x, r_y)$ is the radius of the local bed curvature in the x and y directions; p_{bed} is the basal pore-fluid pressure; $g=(g_x, g_y, g_z)$ is the gravity acceleration in all directions; k_{ap} is the earth pressure coefficient; ϕ_{bed} is the basal friction angle; and ϕ_{int} is the internal friction angle. Interchanging x and y as well as u and v in the x-direction momentum equation yields the following y-direction momentum equation:

$$\rho\left[\frac{\partial(hv)}{\partial t}+\frac{\partial(huv)}{\partial x}+\frac{\partial(hv^2)}{\partial y}\right] = \rho g_y h-\mathrm{sgn}(v)(\rho g_z h-p_{\mathrm{bed}})\left(1+\frac{v^2}{r_y g_z}\right)\tan\phi_{\mathrm{bed}} +\vartheta_f\mu h\frac{\partial^2 v}{\partial x^2}-\mathrm{sgn}\left(\frac{\partial v}{\partial x}\right)hk_{\mathrm{ap}}\frac{\partial(\rho g_z h-p_{\mathrm{bed}})}{\partial x}\sin\phi_{\mathrm{int}} -3\vartheta_f\mu\frac{v}{h}+\vartheta_f\mu h\frac{\partial^2 v}{\partial y^2}-hk_{\mathrm{ap}}\frac{\partial(\rho g_z h-p_{\mathrm{bed}})}{\partial y}-h\frac{\partial p_{\mathrm{bed}}}{\partial y} \tag{3}$$

The depth-integrated pore pressure evolution equation, which takes into account the effect of the shear-induced dilation rate, may be expressed as (Iverson and Denlinger 2001)

$$\frac{\partial p_{\mathrm{bed}}}{\partial t}=-\left(u\frac{\partial p_{\mathrm{bed}}}{\partial x}+v\frac{\partial p_{\mathrm{bed}}}{\partial y}\right)-\frac{2\eta}{\alpha\mu h^2}\left(p_{\mathrm{bed}}-\rho_f g_z h\right) -\rho_f g_z h\frac{1+2k}{3}\left(\frac{\partial u}{\partial x}+\frac{\partial v}{\partial y}\right)-\sqrt{u^2+v^2}\frac{\tan\Psi}{h\alpha} \tag{4}$$

where α is the compressibility; Ψ is the shear-induced dilatancy angle (a property of granular materials that is commonly expressed as an angle, $-\pi/2<\Psi<\pi/2$); η is the hydraulic permeability; and k is a longitudinal normal-stress coefficient that equals 1 if the stress stat is hydrostatic (Iverson and Denlinger 2001).

An active (or passive) state of stress will develop if an element of a material is elongated (or compressed), and the formula for the corresponding state can be derived from the Mohr diagram (McDougall and Hungr 2005):

$$k_{\mathrm{ap}}=2\frac{1\mp\left[1-\cos^2\phi_{\mathrm{int}}(1+\tan^2\phi_{\mathrm{bed}})\right]^{\frac{1}{2}}}{\cos^2\phi_{\mathrm{int}}} \tag{5}$$

here, "−" corresponds to the active state ($\partial u/\partial x+\partial v/\partial y\geq 0$) and "+" to the passive state ($\partial u/\partial x+\partial v/\partial y\leq 0$).

The model equations are hyperbolic for the mass and momentum-conservation. To more directly reflect these properties of the model, Eqs. (1)–(3) were rewritten in a matrix form as follows, by reordering and moving some source terms to the left-hand side:

$$\frac{\partial\mathbf{Q}}{\partial t}+\frac{\partial\mathbf{F}}{\partial x}+\frac{\partial\mathbf{G}}{\partial y}=\mathbf{S}+\mathbf{T}+\mathbf{R} \tag{6}$$

where

$$\mathbf{Q}=\begin{pmatrix}h\\ hu\\ hv\end{pmatrix},\mathbf{F}=\begin{pmatrix}hu\\ hu^2+\frac{g_z k_{\mathrm{ap}}h^2}{2}\\ huv\end{pmatrix},$$

$$\mathbf{G}=\begin{pmatrix}hv\\ huv\\ hv^2+\frac{g_z k_{\mathrm{ap}}h^2}{2}\end{pmatrix}$$

$$\mathbf{T}=\begin{pmatrix}0\\ \frac{\left(h\left(k_{\mathrm{ap}}-1\right)\partial_x p_{\mathrm{bed}}+\vartheta_f\mu h\partial_x^2 u\right)}{\rho}\\ \left(\frac{h\left(k_{\mathrm{ap}}-1\right)\partial_y p_{\mathrm{bed}}+\vartheta_f\mu h\partial_y^2 v}{\rho}\right)\end{pmatrix};$$

$$\mathbf{R}=\begin{pmatrix}0\\ \left(\frac{\vartheta_f\mu h\partial_y^2 u-sgn(\partial_y u)hk_{\mathrm{ap}}\partial_y(\rho g_z h-p_{\mathrm{bed}})\sin\varphi_{\mathrm{int}}}{\rho}\right)\\ \left(\frac{\vartheta_f\mu h\partial_x^2 v-sgn(\partial_x v)hk_{\mathrm{ap}}\partial_x(\rho g_z h-p_{\mathrm{bed}})\sin\varphi_{\mathrm{int}}}{\rho}\right)\end{pmatrix}$$

$$\mathbf{S}=\begin{pmatrix}0\\ g_x h-sgn(u)\left(g_z h-\frac{p_{\mathrm{bed}}}{\rho}\right)\left(1+\frac{u^2}{r_x g_z}\right)\tan\varphi_{\mathrm{bed}}-3\vartheta_f\mu\frac{u}{h\rho}\\ g_y h-sgn(u)\left(\rho g_z h-\frac{p_{\mathrm{bed}}}{\rho}\right)\left(1+\frac{v^2}{r_y g_z}\right)\tan\varphi_{\mathrm{bed}}-3\vartheta_f\mu\frac{u}{h\upsilon}\end{pmatrix}$$

here, we grouped the source terms on the right-hand side of Eq. (6) according to the type of stress, where **S** represents the driving stress that includes the gravitational force and basal shear stresses, **T** represents the longitudinal normal-stress, and **R** represents the transverse shear stresses, all of which are in the x and y directions.

Methods

The hyperbolic character of the governing equations makes finding solutions difficult because it can generate discontinuous and numerical oscillations in finite time. Moreover, the nonlinear character of the equations limits the applicable range of analytical solutions. Therefore, the numerical method used must be able to eliminate these effects. For this purpose, some methods have been put forth such as the method of characteristics (Katopodes and Strelkoff 1978), the finite difference method (Fennema and Chaudhry 1990), and the finite volume method (Jha et al. 1995; Zoppou and Roberts 2000; Fraccarollo et al. 2003; Brufau et al. 2004; Gottardi and Venutelli 2004; Benkhaldoun et al. 2012). The finite volume method is advantageous in that it is robust and can capture the locations of the discontinuities accurately. However, the exact solution of the Riemann problem is less efficient, so a number of approximate Riemann solvers have been constructed to solve the Riemann problem in an efficient manner (Brufau et al. 2004; Liang and Marche 2009; Toro 2009). In this study, the finite volume method and Roe's approximation were used to solve the debris flow problem (Brufau et al. 2004; Toro 2009). To improve the feasibility of this model, we also used the fractional step method (Gottardi and Venutelli 2004). A simple space-splitting type has been adapted and the model equations are divided into two 1-D problems as follows:

$$\frac{\partial \mathbf{Q}}{\partial t}+\frac{\partial \mathbf{F}}{\partial x}=\mathbf{S}_x+\mathbf{T}_x+\mathbf{R}_x \tag{7}$$

$$\frac{\partial \mathbf{Q}}{\partial t}+\frac{\partial \mathbf{G}}{\partial y}=\mathbf{S}_y+\mathbf{T}_y+\mathbf{R}_y \tag{8}$$

After that, the solution at the next time step can be obtained by an efficient step as follows:

$$\mathbf{Q}^{n+1}=L_{x2}\left(\frac{dt}{2}\right)L_{y2}\left(\frac{dt}{2}\right)L_{y1}\left(\frac{dt}{2}\right)L_{x1}\left(\frac{dt}{2}\right)\mathbf{Q}^{n} \tag{9}$$

where L_x and L_y represent the operator in the x and y directions, respectively, and each is executed twice to obtain the solution at the next step (Liang et al. 2006; Ouyang et al. 2014). For L_{x1}, the two-step calculation can be expressed as follows:

Step 1 Solving the homogeneous shallow water equations

First,

$$\frac{\partial \mathbf{Q}}{\partial t}+\frac{\partial \mathbf{F}}{\partial x}=0 \tag{10}$$

The corresponding discretization form of homogeneous operator Eq. (10), which is based on the finite volume method, is written as

$$\mathbf{Q}_i^{n+1}=\mathbf{Q}_i^{n}+\frac{\Delta t}{\Delta x}\left(\mathbf{F}^{n}_{i+\frac{1}{2}}-\mathbf{F}^{n}_{i-\frac{1}{2}}\right) \tag{11}$$

where $\mathbf{F}^{n}_{i+\frac{1}{2}}$ and $\mathbf{F}^{n}_{i-\frac{1}{2}}$ are numerical fluxes at the cell interface. In this paper, the numerical fluxes are solved using Roe's approximation. In Roe's approximation, the nonlinear problem is linearized at the cell interface. At the cell interface, we have a discontinuity with state $\mathbf{U}_{\mathrm{L}}$ on the left side and state $\mathbf{U}_{\mathrm{R}}$ on the right side. Equation (10) is linearized as follows:

$$\frac{\partial \mathbf{Q}}{\partial t}+\mathbf{J}\frac{\partial \mathbf{Q}}{\partial x}=0 \tag{12}$$

Then, the Jacobian matrix $\mathbf{J}$ of the normal flux $\mathbf{F}$ can be evaluated as

$$\mathbf{J}=\frac{\partial \mathbf{F}}{\partial \mathbf{Q}}=\begin{bmatrix}0 & 1 & 0\\ c_m^2-u^2 & 2u & 0\\ -uv & v & u\end{bmatrix} \tag{13}$$

where h, c_m, u, and v for the average state are

$$h=\sqrt{h_L h_R},\ c_m=\sqrt{\frac{1}{2}k_{ap}g_z(h_R+h_L)},\ u=\frac{\sqrt{h_R}u_R+\sqrt{h_L}u_L}{\sqrt{h_R}+\sqrt{h_L}},\ v=\frac{\sqrt{h_R}v_R+\sqrt{h_L}v_L}{\sqrt{h_R}+\sqrt{h_L}} \tag{14}$$

The evaluation of the numerical flux used in this study, derived from Eq. (11), is accomplished with

$$\mathbf{F}=\frac{1}{2}\left[\mathbf{F}_R+\mathbf{F}_L-|\mathbf{J}|(\mathbf{Q}_R-\mathbf{Q}_L)\right] \tag{15}$$

The approximate Jacobian matrix is not directly used in the actual method. Instead, the difference in the vector $\boldsymbol{Q}$ across the grid edge is decomposed on the basis of the matrix eigenvectors as

$$\Delta\mathbf{Q}=\mathbf{Q}_R-\mathbf{Q}_L=\sum_{m=1}^{3}\alpha^m\gamma^m \tag{16}$$

and

$$|\mathbf{J}|(\mathbf{Q}_R-\mathbf{Q}_L)=\sum_{m=1}^{3}(|\lambda^m|\alpha^m\gamma^m) \tag{17}$$

where α represents the wave strengths; λ are eigenvalues of $\mathbf{J}$; and γ are the corresponding eigenvectors.

Step 2 Solving the source term.

After the solution, $\mathbf{Q}^m$ of Eq. (10) is obtained by the above steps with initial date $\mathbf{Q}$, and the source term can be calculated as

$$\frac{\partial \mathbf{Q}}{\partial t}=\mathbf{S}+\mathbf{T}+\mathbf{R} \tag{18}$$

To reduce numerical instabilities, a semi-implicit method is used and the equation is discretized as shown below:

$$\frac{\mathbf{Q}^x-\mathbf{Q}^m}{\Delta t}=\mathbf{S}^m+\mathbf{T}^m+\mathbf{R}^m \tag{19}$$

where $\mathbf{S}^m$, $\mathbf{T}^m$, and $\mathbf{R}^m$ can be obtained by $\mathbf{Q}^m$.

After the solution, $\mathbf{Q}^x$ of Eq. (7) (x-direction) is obtained by the above steps with initial date $\mathbf{Q}^n$, and by solving Eq. (8) (y-direction) with the date $\mathbf{Q}^x$ to obtain the solution $\mathbf{Q}^{n+1}$ through the same steps. Lastly, the pore-fluid pressure p_{bed} can be updated by $\mathbf{Q}^{n+1}$.

The stability criterion adopted here is expressed by (Brufau et al. 2004; Gottardi and Venutelli 2004)

$$\Delta t\le \min\left(cfl\frac{A}{\max(\sqrt{u^2+v^2}+c_m)P}\right) \tag{20}$$

where $cfl<1$ is the Courant number; and A and P are the area and perimeter of the computational cell, respectively.

Results and discussion

A series of model tests were undertaken to verify the presented numerical model. Specifically, the model predictions were compared with alternative numerical solutions and laboratory experimental data published in the literature. The computational grid size was fixed at 5 cm, the gravity acceleration $g=9.8$ m/s^2, and the Courant number $cfl=0.7$. Moreover, free boundary conditions were imposed on each side of the computational domain.

Laboratory dam-break over a triangular hump

In this sub-section, a laboratory dam-break flow over a triangular hump, which was performed by the EU CADAM (European Union Concerted Action on Dam Break Modelling) project, was simulated to verify the accuracy of the current computational framework. The experiment setup is sketched in Fig. 1. The horizontal domain was 38 m long with the gate located 15.5 m away from the upstream end. The still water surface elevation of the reservoir was 0.75 m. A symmetric triangular hump that was 0.4 m high and 6 m long was located 10 m away from the gate at the downstream end. The floodplain was initially dry and a constant Manning coefficient of $n = 0.0125$ was used throughout the domain. The upstream and downstream ends of the domain were assumed to be a solid wall and a free outlet, respectively. Seven gauges were located at 2, 4, 8, 10, 11, 13, and 20 m downstream of the gate, and these were used to record the time history of the water depth, which reflects the complicated process of water wave propagation. By assuming that the gates all open suddenly, the simulation results were computed and then compared to the laboratory measurements; these data are shown in Fig. 2. At those gauges, the arriving time and water depth were predicted with a high amount of precision. Although a small discrepancy was observed at gauge 7 between the numerical and measured values, the comparison between the numerical predictions and measurements was satisfactory at most of the gauge points overall. This confirms the effectiveness of the presented method for practical problem simulation.

Computational results compared with USGS flume experiments

To verify the ability of the current model to capture the debris flow dynamics over non-erodible beds, numerical computational comparisons were made with U.S. Geological Survey (USGS) flume experimental results. The experimental description of the debris flow on the non-erodible bedspread was summarized by Iverson et al. (2010). The computational material parameters and corresponding measured values are listed in Table 1. The value of k varied from about 0.3 to 3 depending on whether the flowing debris underwent longitudinal extension or compression (Iverson 2009; George and Iverson 2011). To focus our computations on the evolution of the debris flow height, the traditional shallow-flow assumption was used, where $k = 1$. Comparisons between the numerical solutions and experimental results for the flow height and pore-fluid pressure versus time are shown in Figs. 3, 4, respectively. The results show that the flow arrival time to the sensor and the flow height versus time agree well with the experimental results. However, a timing discrepancy was observed with respect to the pore-fluid pressure. In the experimental data, the arrival time of pore-fluid pressure was about 1 s late when compared with the arrival time of the flow front. This phenomenon is commonly observed in debris flows because of particle-size segregation during the movement process (Iverson et al. 2010, 2015). It can be concluded that the pore-fluid pressure versus time data agreed well with the experimental results, except for the timing discrepancy.

Predictions of downslope debris flow dynamics

To study the effect of pore-fluid pressure on the motion of debris flow, a simple numerical test was conducted for simulations of debris flow down an inclined slope. A sketch of the chute and the initial shape of the debris flow are shown in Fig. 5. In the numerical test, a simple reference surface was defined, which consisted of an inclined plane (slope angle $= 40°$, $x < 175$ cm), a horizontal run-out zone ($x > 215$ cm), and a transition zone joining the two regions. Superimposed on the inclined section of the chute was shallow, parabolic, and cross-slope topography ($y^2/2R$ with $R = 110$ cm). The flow material was released from rest of the parabolic inclined section of the chute by means of a Perspex cap that opened rapidly ($t = 0$ s). The cap was

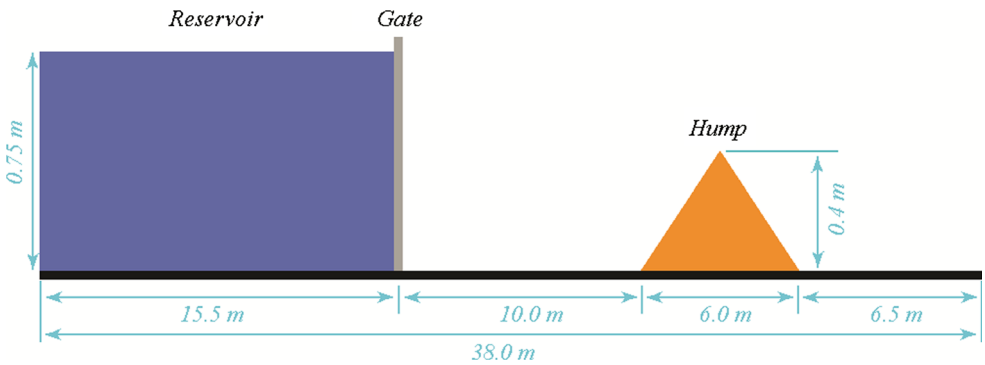

Fig. 1 Dam-break over a hump: experimental setup

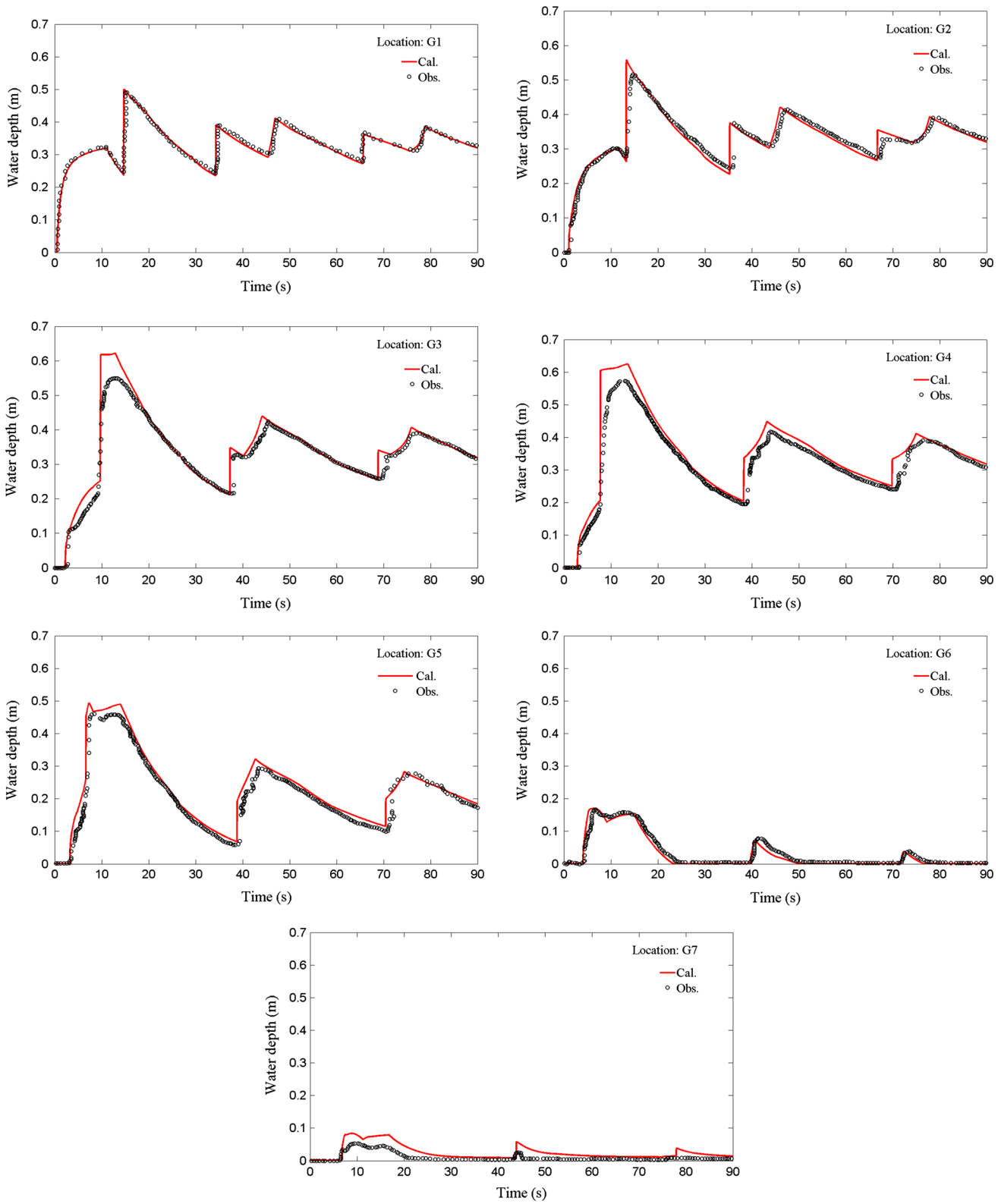

Fig. 2 Dam-break over a hump: time histories of water depth at different gauges

fitted to the basal chute topography and it had a spherical free surface. The major axis of the cap was 32 cm in length, and the maximum height of the cap above the reference surface was 22 cm. The basal friction angle was set to $\phi_{\text{bed}} = 30^{\circ}$ and other computational material parameters were the same as those shown Table 1. The

Table 1 The values of computational parameters

Parameter (units)	Symbol	Experiment value(s)	Model value
Solid phase density (kg/m^3)	ρ_s	2700	2700
Fluid phase density (kg/m^3)	ρ_f	1100	1100
Slope angle (degrees)	δ	31	31
Basal friction angle (degrees)	ϕ_{bed}	40	40
Internal friction angle (degrees)	ϕ_{int}	40	40
Hydraulic permeability (m^2)	η	4×10^{-12} to 4×10^{-11}	4.5×10^{-12}
Pore-fluid viscosity (Pa–s)	μ	0.001 to 0.05	0.005
Compressibility (Pa^{-1})	α	10^{-5} to 10^{-3}	5×10^{-4}
Fluid volume fraction	ϑ_f	<0.4	0.38
Dilatancy angle (radians)	Ψ	−0.2 to 0.2	0.1
Normal-stress coefficient	k	0.3 to 3	1

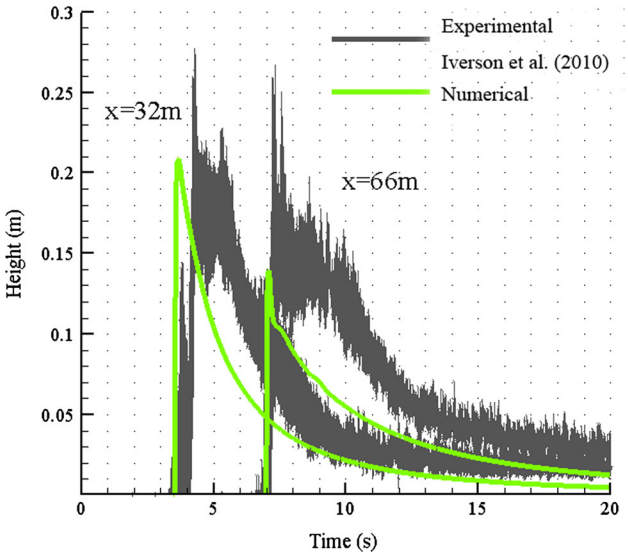

Fig. 3 Comparison of flow height versus time for the flume experiment with a rough bare bed at locations $x = 32$ and 66 m

computed results, which consisted of three representative moments at times $t = 0.51$, 1, and 1.51 s, are shown in Fig. 6. Once the cap was open, the debris flow accelerated and spread out rapidly in the downslope direction. The computed results without pore-fluid pressure were slightly less than those of the computed results with pore-fluid pressure at $t = 0.51$ s, and the distance of later spread with pore-fluid pressure was larger. Owing to the particular cross-slope topography of the chute, the distance of lateral spread of the debris flow during movement was shorter at $t = 1$ s when compared with the shape of debris flow at $t = 0.51$ s. As the debris flow entered the horizontal run-out zone, compared to the debris flow with pore-fluid pressure, the debris flow without pore-fluid pressure began to accumulate at $t = 1$ s. In the end, the differences in sliding distances between the two numerical results were obvious, and the spread areas were also different. These results demonstrate that pore-fluid pressure can counteract normal stresses at grain contacts and reduce friction, thus further enhancing the bulk flow mobility.

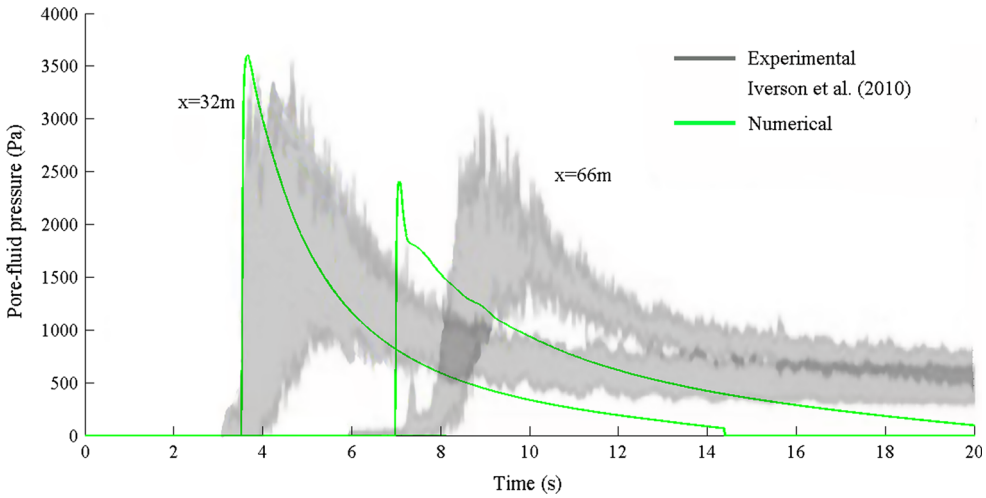

Fig. 4 Comparison of pore-fluid pressure versus time for the flume experiment with a rough bare bed at locations $x = 32$ and 66 m

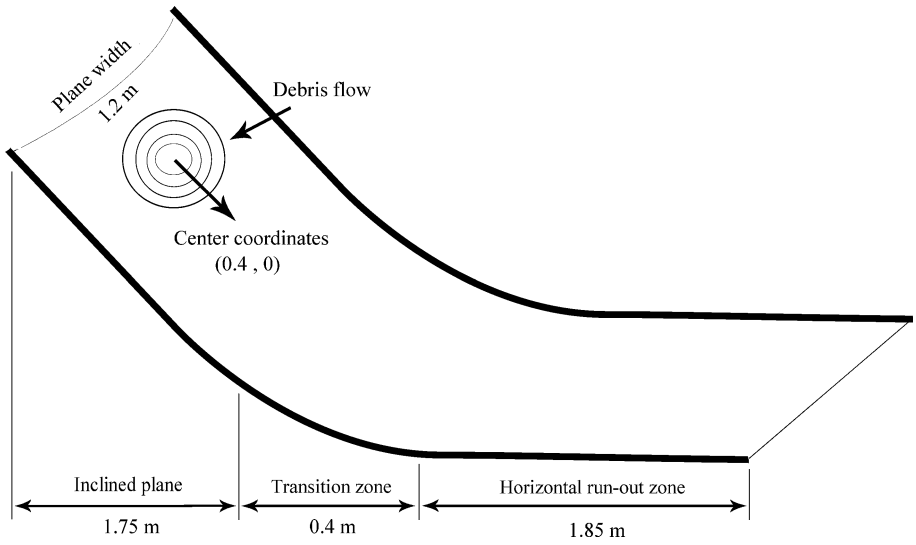

Fig. 5 Simple sketch of the chute and initial shape of the debris flow

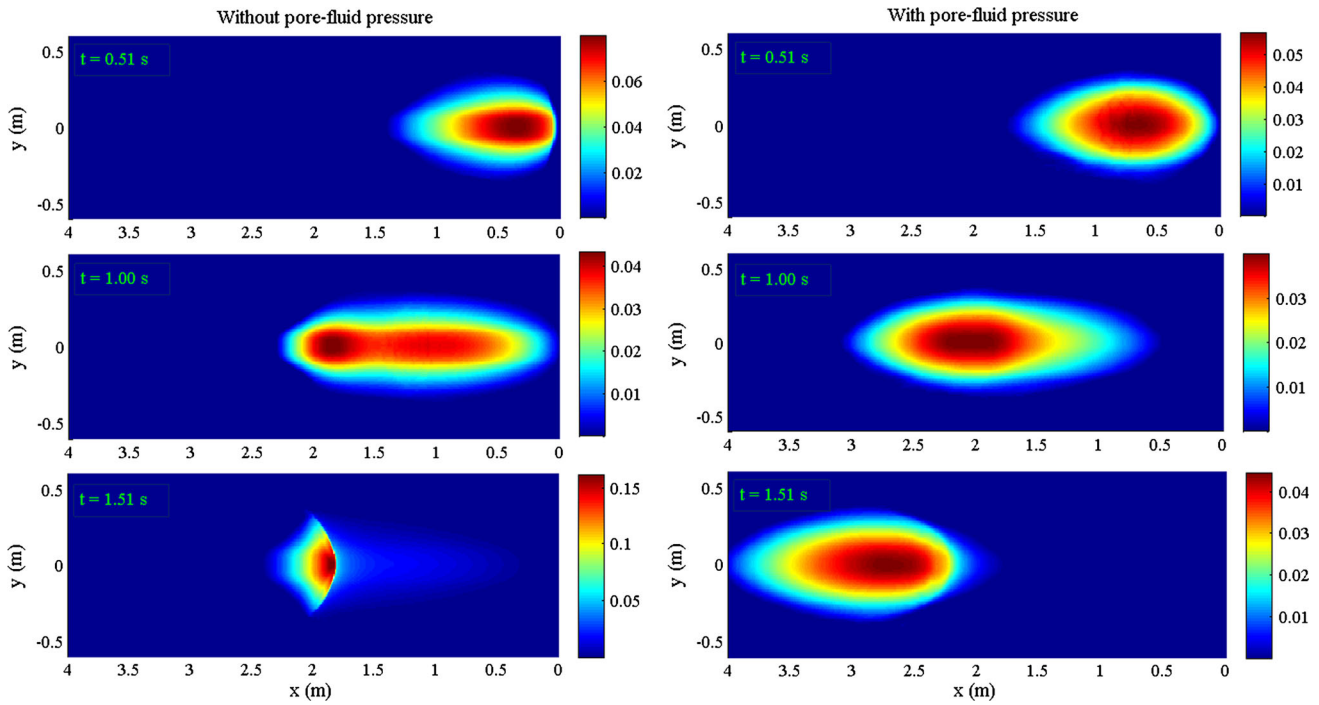

Fig. 6 Comparison of the numerical results between experiments with pore-fluid pressure (*right*) and without pore-fluid pressure (*left*) at three representative moments $t = 0.51$, 1 and 1.51 s

Analysis of debris shear-induced dilatancy

The effect of debris shear-induced dilatancy on the evolution of pore-fluid pressure was also investigated. For this purpose, we performed one numerical test with three different values of $\Psi = -\pi/4, 0, \pi/4$ under the same conditions. The channel was 10 m long, and it consisted of an inclined plane (slope angle = 31°, $x < 4$ m), a horizontal run-out zone ($x > 6$ m), and a transition zone joining the two regions. The initial condition of debris flow at $t = 0$ s is given by

$$u = 0, h = \begin{cases} 0.6(x-1) & 1 \le x \le 1.5m \\ 0.6(2-x) & 1.5 \le x \le 2m \\ 0 & \text{otherwise} \end{cases} \quad (21)$$

The computational parameters were set to a basal friction angle of $\phi_{bed} = 28^{\circ}$, an internal friction angle of $\phi_{int} = 42^{\circ}$, and the other computational material parameters were

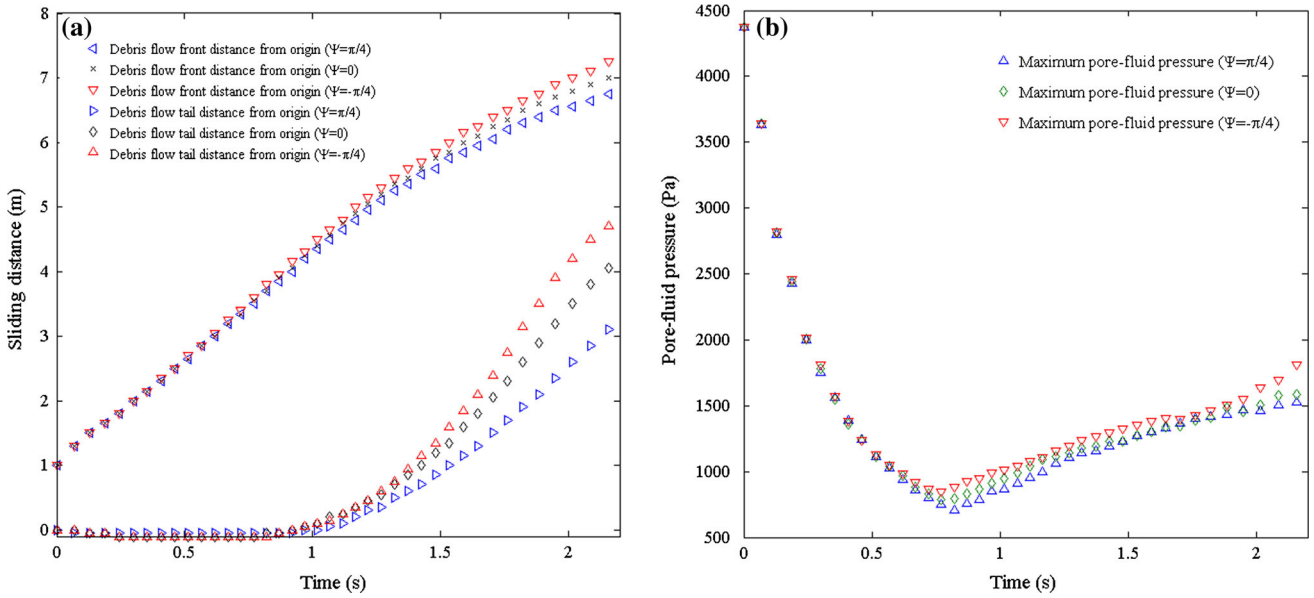

Fig. 7 Simulation of **a** the locations of the debris flow front and tail, and **b** the maximum pore-fluid pressure with increase of time

the same as those in Table 1. In order to illustrate the difference between the numerical results more intuitively, the positions of both the front and tail parts of the landslide as it descended the incline are shown in Fig. 7, along with the maximum pore-fluid pressure during the run. The simulation results show similar overall characteristics. In the numerical tests, the maximum pore-fluid pressure with a smaller dilatancy angle was higher with increase of time than that with a larger dilatancy angle, and this led to a longer sliding distance of debris-flow. It can be concluded that the grains of debris flow converge during shearing because of the negative dilatancy, and the remaining pore-fluid pressure counteracts normal stresses at grain contacts and reduces friction. In contrast, positive dilatancy caused dissipation of pore-fluid pressure, thus further helping to stabilize debris-flow motion.

Conclusions

In this paper, a high-resolution numerical scheme based on the finite volume method was proposed to solve Iverson's two-phase debris flow model. To improve the feasibility of this scheme, the fractional step method was adopted in this study. The numerical method has been programmed, and several numerical experiments were conducted. In these numerical experiments, the influences of factors such as pore-fluid pressure evolution and shear-induced dilatancy on debris flow mobility were considered. By comparing the numerical results with experimental data, the accuracy of the numerical method and the feasibility of the model have been verified. Moreover, the effects of pore-fluid pressure and shear-induced dilatancy on debris flow mobility have been investigated. The results showed that pore-fluid pressure can have marked effects on the mobility of debris flows. Debris shear-induced dilatancy was also found to be an important factor that can influence the evolution of pore-fluid pressure and further affect the motion of debris flows. However, in future studies, it will be necessary to collect more information about the relevant factors that influence the behavior of pore-fluid pressures so that the present model can be calibrated to predict the motion of actual debris flows more accurately.

Acknowledgments The authors greatly appreciate the careful review and helpful comments from anonymous reviewers. Financial support from the National Natural Science Foundation of China (NSFC) (Grant No. 41272346, 41101008) and the National Key Basic Research Program of China (Project No. 2013CB733201) is acknowledged.

References

Anderson TB, Jackson R (1967) Fluid mechanical description of fluidized beds. Equations of motion. Ind Eng Chem Fundam 6(4):527–539

Begueria S, Van Asch TWJ, Malet JP, Grondahl S (2009) A GIS-based numerical model for simulating the kinematics of mud and debris flows over complex terrain. Nat Hazards Earth Syst Sci 9:1897–1909

Benkhaldoun F, Sari S, Seaid M (2012) A flux-limiter method for dam-break flows over erodible sediment beds. Appl Math Model 36(10):4847–4861

Brufau P, García-Navarro P, Vázquez-Cendón ME (2004) Zero mass error using unsteady wetting–drying conditions in shallow flows over dry irregular topography. Int J Numer Methods Fluids 45(10):1047–1082

Fennema RJ, Chaudhry MH (1990) Explicit methods for 2-D transient free surface flows. J Hydraul Eng 116(8):1013–1034

Fraccarollo L, Capart H, Zech Y (2003) A Godunov method for the computation of erosional shallow water transients. Int J Numer Methods Fluids 41(9):951–976

George DL, Iverson RM (2011) A two-phase debris-flow model that includes coupled evolution of volume fractions, granular dilatancy, and pore-fluid pressure. Ital J Eng Geol Environ. In press doi 10 2011–03

Goren L, Aharonov E (2007) Long runout landslides: the role of frictional heating and hydraulic diffusivity. Geophys Res Lett 34:L07301. doi:10.1029/2006GL028895

Goren L, Aharonov E (2009) On the stability of landslides: a thermo-poro-elastic approach. Earth Planet Sci Lett 277(3):365–372

Gottardi G, Venutelli M (2004) Central scheme for two-dimensional dam-break flow simulation. Adv Water Res 27(3):259–268

Gray JMNT, Wieland M, Hutter K (1999) Gravity-driven free surface flow of granular avalanches over complex basal topography. Proceedings of the Royal Society of London A: Mathematical, physical and engineering sciences. The Royal Society 455(1985): 1841–1874

Hsu S, Jaing C, Chen H (2013) Modeling of debris flow using distinct element method. IACGE 2013:713–720. doi:10.1061/9780784413128.082

Hungr O (1995) A model for the run-out analysis of rapid flow slides, debris flows, and avalanches. Can Geotech J 32(4):610–623

Hutter K, Luca I (2012) Two-layer debris mixture flows on arbitrary terrain with mass exchange at the base and the interface. Contin Mech Thermodyn 24(4–6):525–558

Iverson RM (2009) Elements of an improved model of debris-flow motion. Powders and Grains 2009: Proceedings of the 6th International Conference on Micromechanics of Granular Media. AIP Publishing, 1145(1): 9–16

Iverson RM, Denlinger RP (2001) Flow of variably fluidized granular masses across three-dimensional terrain: 1 Coulomb mixture theory. J Geophys Res 106(B1):537–552

Iverson RM, Logan M, LaHusen RG, Berti M (2010) The perfect debris flow? aggregated results from 28 large-scale experiments. J Geophys Res 115:F03005

Iverson RM, George DL, Allstadt K, Reid ME, Collins BD, Vallance JW, Bower JB (2015) Landslide mobility and hazards: implications of the 2014 Oso disaster. Earth Planet Sci Lett 412:197–208

Jha AK, Akiyama J, Ura M (1995) First-and second-order flux difference splitting schemes for dam-break problem. J Hydraul Eng 121(12):877–884

Katopodes ND, Strelkoff T (1978) Computing two-dimensional dam-break flood waves. J Hydraul Division 104(9):1269–1288

Liang Q, Marche F (2009) Numerical resolution of well-balanced shallow water equations with complex source terms. Adv Water Res 32(6):873–884

Liang D, Falconer RA, Lin B (2006) Comparison between TVD-MacCormack and ADI-type solvers of the shallow water equations. Adv Water Res 29(12):1833–1845

Luna BQ, Remaitre A, Van Asch TW, Malet JP, Van Westen CJ (2012) Analysis of debris flow behavior with a one dimensional run-out model incorporating entrainment. Eng Geol 128:63–75

McDougall S, Hungr O (2005) Dynamic modelling of entrainment in rapid landslides. Can Geotech J 42(5):1437–1448

Ouyang C, He S, Xu Q (2014) MacCormack-TVD finite difference solution for dam break hydraulics over erodible sediment beds. J Hydraul Eng 141(5):06014026

Paik J (2015) A high resolution finite volume model for 1D debris flow. J Hydro-environ Res 9(1):145–155

Pitman EB, Le L (2005) A two-fluid model for avalanche and debris flows. Philos Trans Royal Soc London A: Math, Phys Eng Sci 363(1832):1573–1601

Pitman EB, Nichita CC, Patra A, Bauer A, Sheridan M, Bursik M (2003) Computing granular avalanches and landslides. Phys Fluids (1994–present) 15(12):3638–3646

Preh A, Kuen B, Hungr O, Poisel R (2011) Run-up of landslide runouts against protective barriers-a comparison of the particle flow code (PFC) and Dan. The Second World Landslide Forum Abstract, WLF2-2011-0422

Pudasaini SP (2012) A general two-phase debris flow model. J Geophys Res 117:F3

Pudasaini SP, Hutter K (2003) Rapid shear flows of dry granular masses down curved and twisted channels. J Fluid Mech 495:193–208

Savage SB, Hutter K (1989) The motion of a finite mass of granular material down a rough incline. J Fluid Mech 199:177–215

Toro EF (2009) Riemann solvers and numerical methods for fluid dynamics: a practical introduction. Springer Science & Business Media

Wu JH (2010) Seismic landslide simulations in discontinuous deformation analysis. Comput Geotech 37(5):594–601

Wu JH, Chen CH (2011) Application of DDA to simulate characteristics of the Tsaoling landslide. Comp Geotech 38(5):741–750

Wu JH, Lin JS, Chen CS (2009) Dynamic discrete analysis of an earthquake-induced large scale landslide. Int J Rock Mech Min Sci 46(2):397–407

Wu JH, Chen JH, Lu CW (2013) Investigation of the Hsien-du-Shan rock avalanche caused by typhoon Morakot in 2009 at Kaohsiung county Taiwan. Int J Rock Mech Min Sci 60:148–159

Zhang H, Tan Y, Shu S, Niu X, Trias FX, Yang D, Sheng Y (2014) Numerical investigation on the role of discrete element method in combined LBM–IBM–DEM modeling. Comput Fluids 94:37–48

Zhao J, Wang D, Zhang D, Zhang H (2014) Numerical simulation of rainfall-induced rock mass collapse and debris flow. Sci Res Essays 9(19):851–863

Zoppou C, Roberts S (2000) Numerical solution of the two-dimensional unsteady dam break. Appl Math Model 24(7):457–475